Sources of global warming of the upper ocean on decadal period scales

Warren B. White
Scripps Institution of Oceanography, University of California at San Diego, La Jolla, California, USA

Michael D. Dettinger and Daniel R. Cayan
United States Geological Survey, San Diego, California, USA

Received 18 March 2002; revised 13 February 2003; accepted 7 March 2003; published 5 August 2003.

[1] Recent studies find global climate variability in the upper ocean and lower atmosphere during the twentieth century dominated by quasi-biennial, interannual, quasi-decadal and interdecadal signals. The quasi-decadal signal in upper ocean temperature undergoes global warming/cooling of $\sim$0.1°C, similar to that occurring with the interannual signal (i.e., El Niño–Southern Oscillation), both signals dominated by global warming/cooling in the tropics. From the National Centers for Environmental Prediction troposphere reanalysis and Scripps Institution of Oceanography upper ocean temperature reanalysis we examine the quasi-decadal global tropical diabatic heat storage (DHS) budget from 1975 to 2000. We find the anomalous DHS warming tendency of 0.3–0.9 W m^{-2} driven principally by a downward global tropical latent-plus-sensible heat flux anomaly into the ocean, overwhelming the tendency by weaker upward shortwave-minus-longwave heat flux anomaly to drive an anomalous DHS cooling tendency. During the peak quasi-decadal warming the estimated dissipation of DHS anomaly of 0.2–0.5 W m^{-2} into the deep ocean and a similar loss to the overlying atmosphere through air-sea heat flux anomaly are balanced by a decrease in the net poleward Ekman heat advection out of the tropics of 0.4–0.7 W m^{-2}. This scenario is nearly the opposite of that accounting for global tropical warming during the El Niño. These diagnostics confirm that even though the global quasi-decadal signal is phase-locked to the 11-year signal in the Sun's surface radiative forcing of $\sim$0.1 W m^{-2}, the anomalous global tropical DHS tendency cannot be driven by it directly. *INDEX TERMS:* 3339 Meteorology and Atmospheric Dynamics: Ocean/atmosphere interactions (0312, 4504); 4572 Oceanography: Physical: Upper ocean processes; 7536 Solar Physics, Astrophysics, and Astronomy: Solar activity cycle (2162); 1620 Global Change: Climate dynamics (3309).

Citation: White, W. B., M. D. Dettinger, and D. R. Cayan, Sources of global warming of the upper ocean on decadal period scales, *J. Geophys. Res.*, *108*(C8), 3248, doi:10.1029/2002JC001396, 2003.

1. Introduction

[2] *Allan* [2000], *White and Cayan* [2000], and *Tourre et al.* [2001] computed spectra for sea surface temperature (SST) and sea level pressure (SLP) anomalies over the Global Ocean, the Indo-Pacific Ocean, and the Pacific Ocean, respectively, over the twentieth century, finding significant peaks for a quasi-biennial signal near 2.2-year period, four interannual signals near 2.8- 3.5-, 5.4-, and 7-year period, and a quasi-decadal signal near 11-year period. These quasiperiodic signals are similar to those observed by *Mann and Park* [1996] and *Lau and Weng* [1995] in covarying surface temperature and SLP anomalies occurring over the northern hemisphere during the past century. Both *Allan* [2000] and *Tourre et al.* [2001] found the signals in these three frequency bands sharing similar patterns and evolution in covarying SST and SLP anomalies over the Global Ocean and Pacific Ocean, respectively. Yet, subtle differences in these patterns suggest dynamical consequences. For example, the meridional scale of equatorial SST and zonal surface wind (ZSW) anomalies increases with increasing period scale. So, *White et al.* [2003] examined the evolution of quasi-biennial, interannual, and quasi-decadal signals in upper ocean temperature and surface wind in the Pacific Ocean, finding all three evolving in similar fashion and sharing a delayed action oscillator (DAO) mechanism similar to that used to explain the quasiperiodicity of El Niño [e.g., *Zebiak and Cane*, 1987]. They found the increasing meridional scale of equatorial SST and ZSW anomalies with increasing period scale associated with the Ekman pumping of off-equatorial Rossby waves of increasing meridional scale. The latter is responsible for the three different signals in the DAO model. Thus the quasi-biennial, interannual, and quasi-decadal signals that dominate climate variability in the Pacific basin appear to be natural ocean-atmosphere coupled modes of the basin. Thus it should not be surprising that the

0148-0227/03/2002JC001396$09.00

pattern and evolution of the quasi-decadal signal are similar to those associated with the interannual signals of the El Niño–Southern Oscillation (ENSO) [*Tourre et al.*, 2001].

[3] Yet, quasi-decadal basin- and global-averaged SST's have been observed fluctuating in phase with the ~11-year signal in the Sun's irradiance from 1900 to 1995 [*White et al.*, 1997], with a global-averaged SST signal of ~0.1°C (and standard error of ~0.01°C) associated with Sun's surface radiative forcing of ~0.1 W m^{-2}. *White et al.* [1997] found the global-averaged quasi-decadal SST signal dominated by the global tropical average, penetrating no deeper than to the top of the main pycnocline. Subsequently, *White et al.* [1998] examined quasi-decadal changes in the diabatic heat storage (DHS) of this upper layer, computing the depth-averaged temperature (DAT) changes from the sea surface to the top of the main pycnocline. Diagnosing a one-dimensional global model of the quasi-decadal global tropical DHS budget from 1955 to 1995, they found the corresponding DAT anomalies of ~0.06°C to be about twice those expected from the transient Stefan-Boltzmann (S-B) radiation balance for the Earth's surface, with the upper ocean unable to come into radiation equilibrium with the Sun's ~11-year signal. Since the observed magnitude (phase) of the global tropical quasi-decadal DAT signal was larger (smaller) than expected from the transient S-B physics, they deduced that the quasi-decadal global warming/cooling of the upper ocean could not be explained by the Sun's direct surface radiative forcing.

[4] Subsequently, *White et al.* [2001] found the global interannual signals (i.e., ENSO) also associated with global tropical warming/cooling (i.e., ~0.15°C), occurring in the absence of corresponding interannual signals in the Sun's irradiance. They found the anomalous global tropical DHS warming tendency driven by a reduction in tropical trade winds, reducing the net meridional Ekman heat advection out of the tropics. Subsequently, during the peak warm phase (i.e., El Niño), the warm global tropical DAT anomalies drove a sensible-plus-latent heating of the overlying atmosphere. These results suggested that Earth's natural quasi-decadal signal is quite capable of producing basin- and global-averaged DAT changes of O(0.1°C) independent of the ~11-year signal in the Sun's surface radiative forcing. They also indicated that the question concerning how the ~11-year signal in the Sun's irradiance drives the Earth's global-averaged upper ocean temperature should be restated; that is, how does the quasi-decadal signal in the Sun's irradiance excite the Earth's natural quasi-decadal signal?

[5] In the present study, we seek to understand how the Earth's quasi-decadal signal produces global warming/cooling, beyond any expectations stemming from changes in the Sun's irradiance [*White et al.*, 1998]. We determine whether this differs from the way in which the Earth's interannual signal of the El Niño–Southern Oscillation (ENSO) produces global warming/cooling [*White et al.*, 2001]. To accomplish this, we diagnose the anomalous global-averaged DHS budget of the quasi-decadal signal for the upper ocean over the 25 years from 1975 to 2000, when both the global ocean and the atmosphere were relatively well sampled from 40°S to 60°N. We focus on the global tropical DHS budget from 30°S to 30°N because it explains most if not all of the global warming from 40°S to 60°N. We utilize the National Centers of Environmental Prediction (NCEP) tropospheric reanalysis data set [*Kalnay et al.*, 1996] and the Scripps Institution of Oceanography (SIO) upper ocean temperature reanalysis data set [*White*, 1995] to diagnose the anomalous global tropical DHS budget. We compute the DHS variable from the sea surface down to the depth of the 22°C isotherm embedded in the main pycnocline, outcropping into the near-surface mixed layer near 30° latitude. This follows from the work of *Kleeman et al.* [1999], who proposed that subtropical subduction carries upper layer water into the upper portion of the main pycnocline throughout the tropics, perhaps accounting for the quasi-decadal signal. The anomalous global tropical DHS tendency derives from 3 principal heating sources; that is, the global tropical net air-sea heat flux, the net meridional heat advection between the tropics and extratropics (that is, across the 30° latitude zonal boundaries extending around the globe), and the dissipation of global tropical DHS anomalies via cross-isopycnal mixing into the deep ocean [*White et al.*, 2001].

2. Data and Methods

[6] We utilize 13 variables from 3 sources over the 25-year record from 1975 to 2000. This includes DHS from the SIO upper ocean temperature reanalysis [*White et al.*, 2001]. It includes SST, specific humidity (SpH), cloud fraction (ClF), zonal surface wind (ZSW), the total air-sea heat flux (Q_T) and its latent (Q_E), sensible (Q_S), shortwave radiative (Q_{SW}), and longwave radiative (Q_{LW}) components, and the zonal and meridional momentum fluxes (τ^x, τ^y) across the air-sea interface from the NCEP reanalysis [*Kalnay et al.*, 1996]. Also, it includes irradiance estimates (S) from the Naval Research Lab (NRL) [*Lean et al.*, 1995a]. We analyze the SIO DHS anomalies and the NCEP SST, SpH, ClF, ZSW and Q_T, Q_E, Q_S, Q_{SW}, Q_{LW}, τ^x, and τ^y anomalies together over the global ocean from 30°S to 60°N on decadal period scales. The net heat flux anomaly Q_T is computed as follows; $Q_T = Q_{SW} - Q_{LW} - Q_E - Q_S$, so that Q_T is positive when directed into the ocean, with the same sign as Q_{SW} anomalies but of opposite sign as Q_{LW}, Q_E, and Q_S which are positive directed out of the ocean. Anomalies were constructed by subtracting monthly mean estimates from long term monthly means over the 25-year record.

[7] Here, we define DHS and DAT anomalies differently than in *White et al.* [1998]. In the earlier study, the DHS anomaly (that is, $\rho_O C_{PO} T' \overline{H}$) was computed as the anomalous temperature (T') vertically averaged over the upper layer of the ocean from the sea surface down to an isotherm at the top of the main pycnocline (the DAT anomaly), weighted by the mean depth ($\overline{H}$) of that isotherm at each grid point and the product of seawater density (ρ_O) and the specific heat of water (C_{PO}). In the present study, we redefine this earlier definition of DHS and DAT anomalies by vertically averaging T' from the sea surface down to the depth of the 22°C isotherm (see Appendix A). Moreover, in forming the global tropical average DHS and DAT anomalies, we multiply them by a factor of 1.5 in response to the mismatch between global tropical NCEP SST and SIO SST anomalies (see Appendix B).

[8] The observation of relatively narrow-band quasi-biennial, interannual, quasi-decadal, and interdecadal signals in the Global Ocean and Pacific Ocean SST and SLP

data sets over the twentieth century [*Allan*, 2000; *Tourre et al.*, 2001] at 2.2-, 2.8-, 3.5-, 5.4-, 7-, 11-, and 15–20-year periods allows us to isolate the quasi-decadal signal from the others. Thus we band-pass filter the time sequences of monthly anomalies from 1975 to 2000 using a period admittance window with half-power points at 9 to 13 years, respectively [*Kaylor*, 1977]. Prior to band-pass filtering, we applied maximum entropy spectral analysis [*Andersen*, 1974] to reduce loss of data at the ends of each 25-year time sequence because of low-pass filtering. Thus maximum entropy spectral coefficients were used to extend the time sequences by an amount equal to half the filter width on both ends of the record. This extension allows the half-power point criterion to be preserved in the frequency response function, and it allows over half the variance of the signal near the end points of the record to be faithfully represented [*White*, 2000]. Even though the filter response function of *Kaylor* [1977] is flat, with steep sides and negligible side lobes, the narrow-band quasi-decadal signal at 11-year period may be modified by the relatively narrow-band interannual signal at 7-year period and the more broadband interdecadal signal at 15–20-year period. Thus, in subsequent analysis of the band-pass-filtered quasi-decadal anomalies we remain vigilant for this potential source of contamination. Over the 25-year record, band-pass filtering yields 2–3 cycles of quasi-decadal variability with ~6 effective temporal degrees of freedom at each grid point [*Snedecor and Cochran*, 1980], effectively reducing the subsequent investigation to a case study.

[9] For information about solar irradiance changes over the past century, we turn to *Lean et al.* [1995a], who constructed a solar irradiance time sequence based on a statistical model calibrated with space-based measurements of solar radiative output over the 16 years from 1979 to 1994, recently updated on the World Wide Web to 1999. Estimates earlier than the modern epoch derive from a reconstruction based on knowledge of sources of irradiance variability deduced from extant radiometry, extended in time using parameterizations with appropriate solar activity proxies. The 11-year quasiperiodic solar irradiance cycle occurs because of the combination of bright solar faculae and dark spots, which modulate the Sun's radiation. This allows the irradiance to be reconstructed since 1874 from calculations of sunspot darkening and faculae brightening obtained from ground-based white light solar images. Estimates of global-averaged values at the sea surface (i.e., surface radiative forcing) are smaller than the total irradiance at the top of the atmosphere by a factor of 4 (i.e., because of averaging over the Earth's surface) and by an additional factor of 30% because of reflections associated with cloud and surface albedos [e.g., *Reid*, 1991].

3. Error Analysis

[10] A major question in this study is whether standard errors in monthly DHS anomalies of $\sim 3.0 \times 10^8$ W-s m^{-2} (that is, corresponding to ~0.4°C error in DAT anomalies) can be reduced enough in global and tropical averages to resolve quasi-decadal anomalies of $\sim 2 \times 10^7$ W-s m^{-2} (~0.1°C in DAT). Errors in area averages decrease from those in individual estimates in proportion to the inverse square root of the number of independent estimates [e.g., *Young*, 1962]. Therefore, if we considered each monthly grid point estimate to be independent, then errors in basin and global averages would be less than grid point errors by 2–3 orders of magnitude. However, *White* [1995] determined that individual grid point estimates of upper ocean temperature variability in the SIO reanalysis are not independent, with anomalous variability dominated by decorrelation scales ranging from 3 to 6 months, 2.5° to 5° latitude, and 5° to 10° longitude, smaller in the Atlantic and Indian oceans than in the Pacific Ocean. As such, *White et al.* [1997] determined that ~90, ~50, and ~30 independent estimates occur in the Pacific, Atlantic, and Indian oceans (40°S to 60°N), respectively, every 3 months. This result yields a conservative estimate for standard errors in basin-averaged monthly diabatic heat storage anomalies, ranging from 0.2×10^8 to 0.4×10^8 W-s m^{-2} (0.04° to 0.08°C in DAT). These errors are subsequently reduced by of factor of 5 (i.e., 0.04×10^8 to 0.08×10^8 W-s m^{-2} and 0.01°–0.02°C in DAT) in computing band-pass changes that detect the quasi-decadal signal (i.e., assuming four independent estimates per year). Global-averaged errors are reduced from basin-averaged errors by nearly another factor of 2, reducing standard errors conservatively to $\sim 0.4 \times 10^7$ W-s m^{-2} in DHS and ~0.01°C in DAT when weighted by area. These standard errors are about half an order of magnitude smaller than the magnitude of global-averaged quasi-decadal DHS and DAT anomalies.

[11] A similar exercise can be conducted with the standard errors in the air-sea heat flux anomalies, with monthly mean estimates accurate to within ±20 W m^{-2} [*Cayan*, 1992]. In this case, averaging over each basin yields standard errors ranging from 2 to 4 W m^{-2}. Running these estimates through the quasi-decadal band-pass filter further reduces them to 0.4–0.8 W m^{-2}. Subsequently, global averaging reduces them to ~0.3 W m^{-2}. Again, these standard errors are about 1/3 the magnitude of global tropical air-sea heat flux anomalies of ~1.0 W m^{-2}. Also, they are larger than the intensity of the surface radiative forcing of ~0.1 W m^{-2} associated with ~11-year signal in the Sun's irradiance [*Lean et al.*, 1995a]. This consigns the latter to the noise level of the global tropical air-sea heat flux anomaly.

4. Time Sequences of Global Average Quasi-decadal SST and DAT Anomalies

[12] We find the quasi-decadal signal in global-averaged SST anomalies from 40°S to 60°N ranging over ±0.12°C (Figure 1a), largest at the beginning of the record and decreasing toward the end. As we shall see, this decrease in the magnitude of the quasi-decadal signal over the 25-year record is consistent with anomalous global tropical DHS budget, indicating that it is natural and not because of biases in the observations (also see Appendix B). This quasi-decadal signal in global-averaged SST is dominated by that in the tropics, averaged from 30°S to 30°N, the latter ranging over ±0.14°C (Figure 1b). This is matched by the quasi-decadal signal in global tropical DAT anomalies (Figure 1b), indicating that the global tropical SST signal extends vertically to the depth of the 22°C isotherm. In both time sequences (Figure 1b), global tropical warm SST and DAT anomalies occurred during 1980, 1990, and 2000,

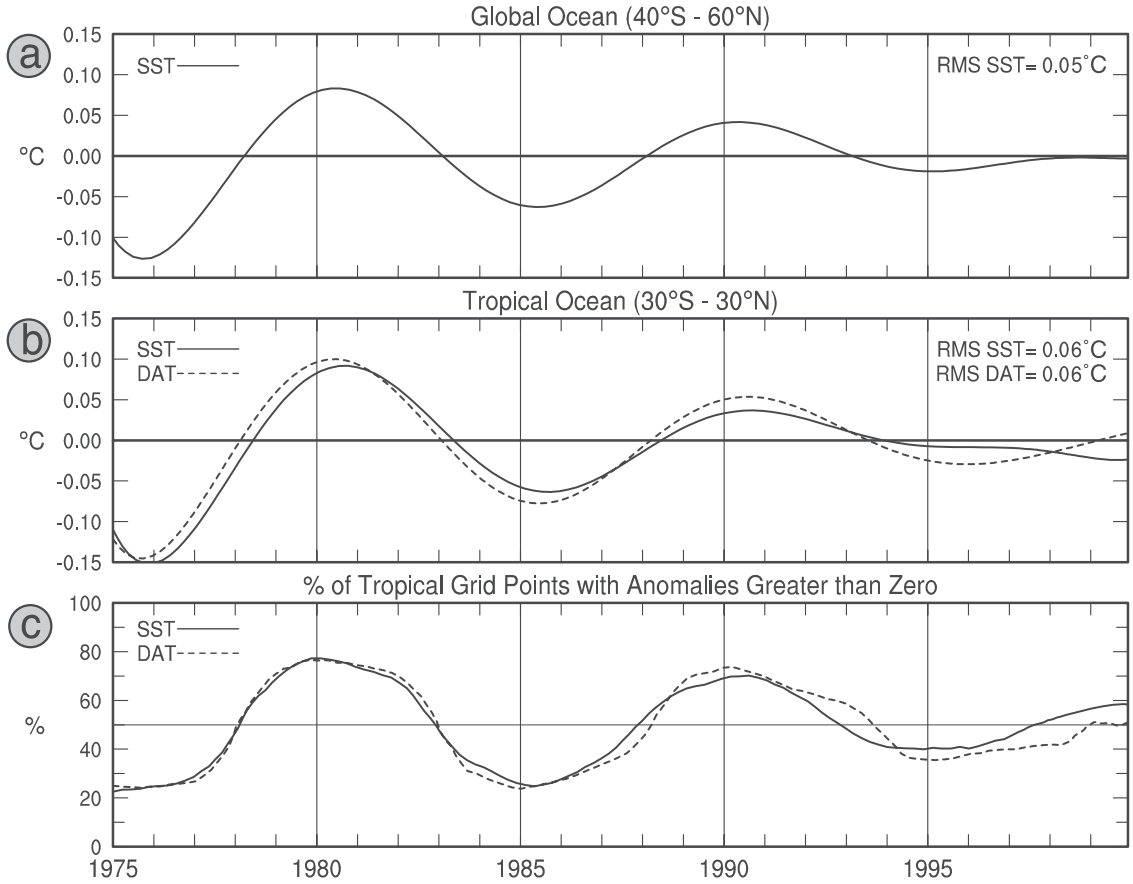

Figure 1. (a) Time sequences of global-averaged NCEP sea surface temperature (SST) anomalies from 40°S to 60°N. (b) Time sequences of global tropical SIO SST anomalies and SIO depth-averaged temperature (DAT) anomalies in the upper layer above the 22°C isotherm from 30°S to 30°N. (c) Time sequences of the percentage of grid points in the tropical global ocean that have warmer than normal SST and DAT anomalies.

while global tropical cool anomalies occurred during 1975, 1985, and 1995, in sync with the ~11-year signal in the Sun's irradiance [*White et al.*, 1997, 1998].

[13] *White et al.* [1997, 1998] found the tropical distribution of SST and DAT anomalies during quasi-decadal global warming to be distributed more uniformly across the tropical Indian, Pacific, and Atlantic oceans than observed on interannual period scales, where ~1/2 the global warming occurred in the eastern equatorial Pacific Ocean associated with the intense local warming associated with El Niño [*White et al.*, 2001]. To confirm this, we construct the time sequence of the percentage of grid points from 30°S to 30°N with anomalies greater than zero. This finds 70% to 80% of grid points across the global tropical ocean warmer than normal during tropical warming of 1980 and 1990 (Figure 1c).

5. Geographical Distributions of the RMS of Quasi-decadal DHS, SpH, CLF, and ZSW Anomalies

[14] The distributions of the root mean square (RMS) of quasi-decadal DHS, SpH, ClF, and ZSW anomalies reveal their magnitude over the global ocean from 30°S to 60°N (Figure 2). A portion of the DHS record can be seen missing in the eastern South Pacific and South Atlantic oceans because of the lack of consistent sampling there. The RMS of quasi-decadal DHS anomalies (Figure 2a) finds maximum variability of 6.0×10^7 W-s m^{-2} in the western and central tropical Pacific Ocean and in the western tropical North Atlantic Ocean, much weaker in the Indian and South Atlantic oceans. The RMS of quasi-decadal SpH anomalies (Figure 2b) finds maximum variability 0.20 g kg^{-1} occurring in the central and eastern tropical Pacific Ocean, half this magnitude in the Indian and Atlantic oceans. The RMS of quasi-decadal ClF anomalies (Figure 2c) has maximum variability of 1.8% in the stratus deck in the subtropical eastern Indian, Pacific, and Atlantic oceans. The RMS of quasi-decadal ZSW anomalies (Figure 2d) achieves maximum variability of 0.35 m s^{-1} in the southeast trade winds in the western and central tropical Pacific Ocean, much weaker in the Indian and Atlantic oceans. Maximum ZSW variability in the western and central tropical Pacific Ocean coincides with that in DHS variability.

6. Evolution of Quasi-decadal DHS, SpH, CLF, and ZSW Anomalies

[15] Applying extended empirical orthogonal function (EEOF) analysis to quasi-decadal DHS, SpH, ClF, and

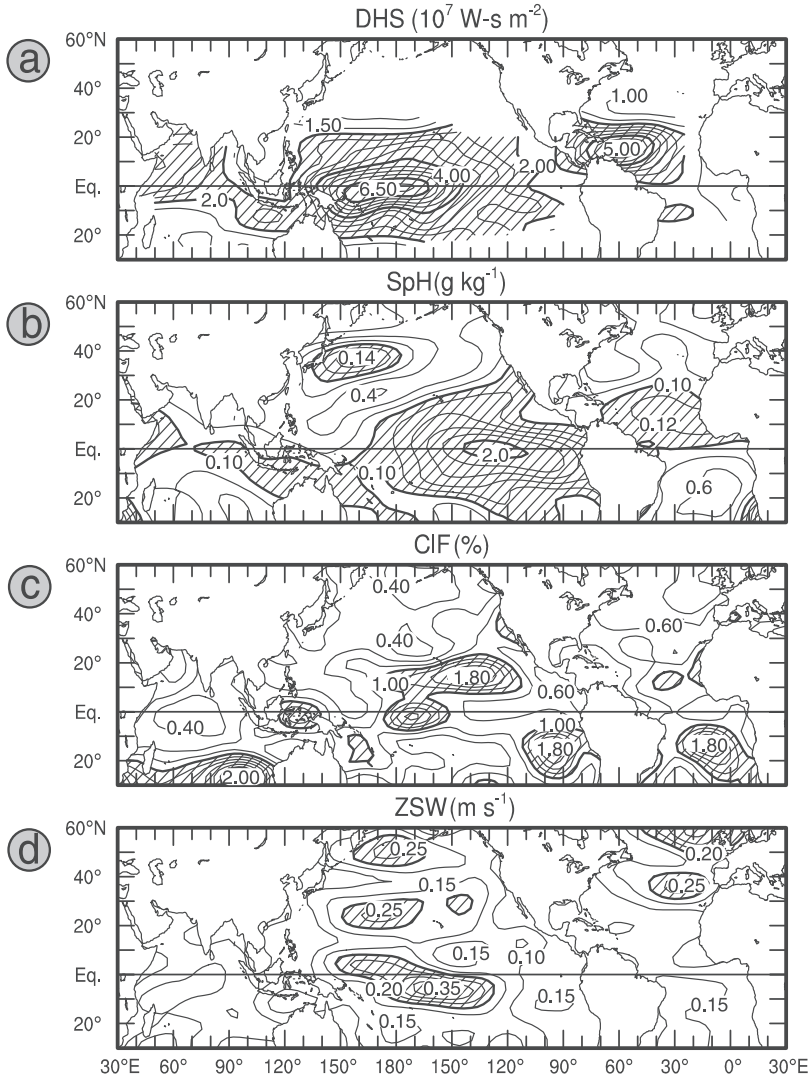

Figure 2. The geographical distribution of the RMS of quasi-decadal anomalies of (a) diabatic heat storage (DHS), (b) specific humidity (SpH), (c) cloud fraction (ClF), and (d) zonal surface wind (ZSW) over the global ocean from 30°S to 60°N. Hatched (unhatched) regions indicate where quasi-decadal changes exceed 2.0×10^7 W-s m^{-2}, 0.10 grams kg^{-1}, 1.0%, and 0.20 m s^{-1}, respectively. Contour intervals are 0.5×10^7 W-s m^{-2}, 0.02 grams kg^{-1}, 0.2%, and 0.05 m s^{-1}, respectively.

ZSW anomalies over the globe [*Weare and Nasstrom*, 1982] reveals how these variables evolve as the Earth's quasi-decadal signal evolves from its tropical cool phase to its tropical warm phase. We conduct EEOF analysis on DHS anomalies from 30°S to 30°N and on the other variables from 30°S to 60°N over the 25-year record (Figure 3). These first EEOF modes account for 93%, 94%, 94%, and 96% of the quasi-decadal variance in DHS, ClF, SpH, and ZSW anomalies, respectively, over the available record. From inspection of the amplitude time sequences for these first EEOF modes (Figure 3a), we find them coinciding, with the four time sequences displaying peaks at the beginning of 1980 and 1990. This correspondence among the four variables occurs without having to force the issue by conducting a joint EEOF analysis on the four variables. Corresponding EEOF lag sequences (Figure 3b) extend over 1/2 cycle of quasi-decadal variability over 6 lag years, displaying the dominant temporal and spatial evolution of the quasi-decadal signal occurring on average over the 25-year record. When the distributions of weights in lag year 3 are multiplied by the time sequences of amplitudes, most of the quasi-decadal variability in the original animation sequences is recovered.

[16] The lag sequence of DHS weights evolves from the tropical cool phase in lag year 0 to the tropical warm phase in lag year 5 (Figure 3b (left)). During the tropical warm phase, the global tropical ocean from approximately 20°S to 30°N is dominated by warm DHS weights, the distribution of which can be seen to be nearly identical to that of moist SpH weights (Figure 3b (middle left)). This indicates that the moisture content in the lower troposphere is anomalously high (low) over warm (cool) DHS anomalies. Even so, the global-average DHS and SLP weights can be seen peaking during lag year 3, ~2 years before the tropical warm phase.

[17] On the other hand, the lag sequence of ClF weights in the tropical atmosphere (Figure 3b (middle right)) evolves from positive ClF weights in lag year 0 to negative

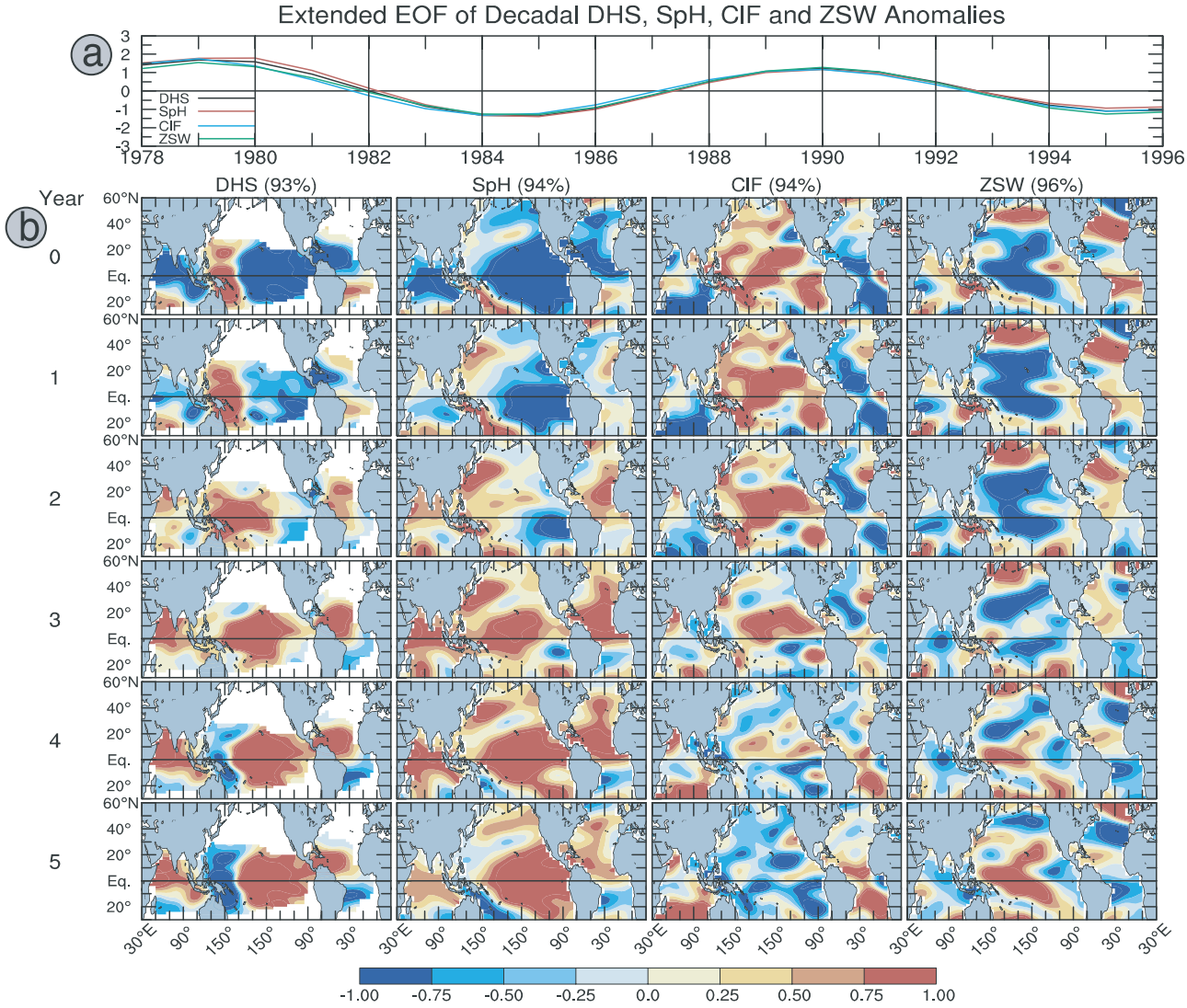

Figure 3. (a) Amplitude time sequences of the dominant extended empirical orthogonal function (EEOF) modes for quasi-decadal DHS, SpH, ClF, and ZSW anomalies from 1978 to 1996. (b) Corresponding lag sequences of the dominant EEOF modes for quasi-decadal DHS, SpH, ClF, and ZSW anomalies. Yellow-to-red (blue) color indicates the contours of positive (negative) weights, multiplied by 1.0×10^7 W-s m^{-2} for DHS weights, 0.2 grams kg^{-1} for SpH weights, 3% for ClF weights, and 0.5 m s^{-1} for ZSW weights. These dominant modes account for 93, 94, 94, and 96% of the global quasi-decadal variance, respectively, over the 25-year record.

ClF weights in lag 6 5, fluctuating nearly out of phase with the DHS and SpH weights. Since less cloud cover increases the incoming shortwave radiative flux (while increasing the outgoing longwave radiative flux), the presence of negative ClF weights during the tropical warm phase may act either to maintain the DHS weights or to diminish them depending on which of the two radiative terms dominates. This issue is resolved below when we diagnose the anomalous global tropical DHS budget.

[18] The lag sequence of ZSW weights in the tropical trade wind system (Figure 3b (right)) evolves from mostly negative ZSW weights in lag year 1 to mostly positive ZSW weights in lag year 6 (the latter not shown). This indicates that the trade wind intensity during and following the tropical warm (cool) phase is weaker (stronger) than normal. Since the intensity of the trade winds is related to the anomalous net meridional Ekman heat advection from the tropics to the extratropics, the latter can be expected to decrease (increase) during and following the tropical warm (cool) phase. This can help maintain the DHS anomalies during the tropical warm (cool) phase against dissipation into the deep ocean via cross-isopycnal mixing and against the loss of heat to the atmosphere via SST-driven sensible-plus-latent heat flux anomalies [*White et al.*, 2001].

7. Global Tropical Quasi-decadal DHS, SpH, CLF, and ZSW Anomalies

[19] Next we quantify the magnitude of global tropical quasi-decadal DHS, SpH, ClF, and ZSW anomalies and relate their phases to one another and to the 11-year signal in the Sun's surface radiative forcing (S) (Figure 4). The range of

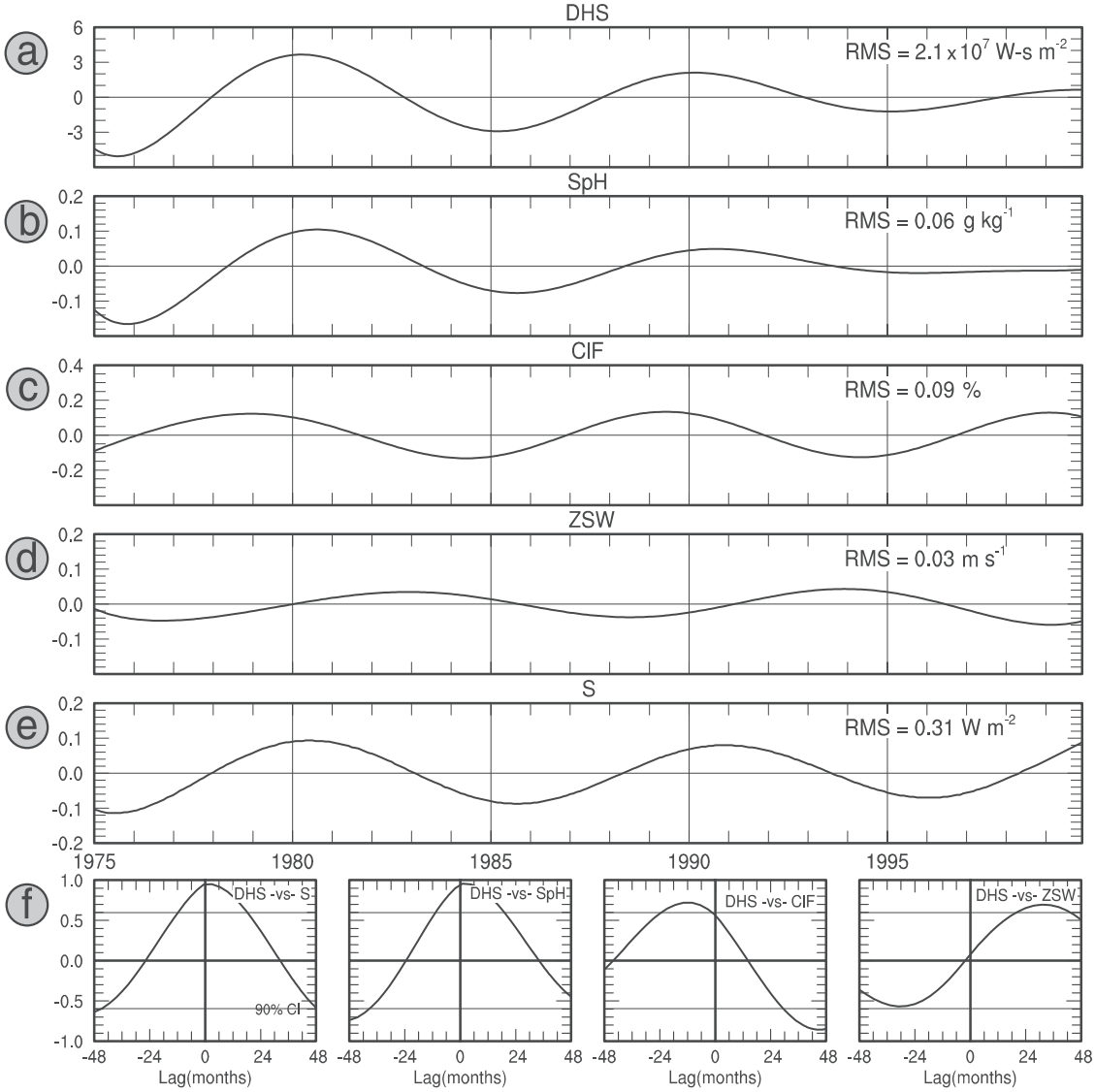

Figure 4. Time sequences of global tropical quasi-decadal anomalies of (a) DHS, (b) SpH, (c) ClF, (d) ZSW, and (e) S over the 25-year record. (f) Temporal lag cross correlations are computed between DHS anomalies and S, SpH, ClF, and ZSW anomalies, with ~6 effective degrees of freedom assigned to the 90% confidence level of 0.6 [*Snedecor and Cochran*, 1980].

global tropical DHS, SpH, ClF, ZSW, and S anomalies is $\pm 5.0 \times 10^7$ W-s m^{-2}, ± 0.14 g kg^{-1}, $\pm 0.2\%$, ± 0.35 m s^{-1}, and ± 0.1 W m^{-2}, respectively. We find the time sequences of global tropical DHS, SpH, and S anomalies fluctuating approximately in phase with one another, with peaks near 1980, 1990, and 2000 (Figures 4a, 4b, and 4e). Temporal lag cross correlations between global tropical DHS and S anomalies show them correlated positively at 0.95, with no significant lead or lag (Figure 4f). Temporal lag cross correlations between global tropical DHS and SpH anomalies shows them also correlated positively at 0.95, again with no significant lead or lag (Figure 4f). Yet, peak global tropical ClF anomalies can be seen leading warm global tropical DHS anomalies by ~1 year (Figures 4a and 4c), confirmed by the temporal lag cross correlation (Figure 4f). Also, the negative global tropical ZSW anomalies can be seen leading warm global tropical DHS anomalies by 2 to 3 years (i.e., ~90° of phase) (Figures 4a and 4d), also confirmed by the temporal lag cross correlation (Figure 4f). This indicates that global tropical trade winds were more intense during the onset of peak tropical warming, as inferred from the EEOF ZSW mode (Figure 3b). This is opposite of that observed on interannual period scales [*White et al.*, 2003], where the global tropical trade winds weakened during the onset of peak tropical warming.

8. Global Tropical Quasi-decadal DHS Budget

[20] Now we diagnose the budget of global tropical DHS anomalies on decadal period scales. The anomalous DHS tendency is driven by three principal heating/cooling mechanisms. The first is the net air-sea heat flux anomaly. The second is the dissipation of DHS anomaly due to cross-isopycnal mixing at the depth of the 22°C isotherm, embedded in the main pycnocline. The third is the net meridional heat advection anomaly across 30°S and 30°N.

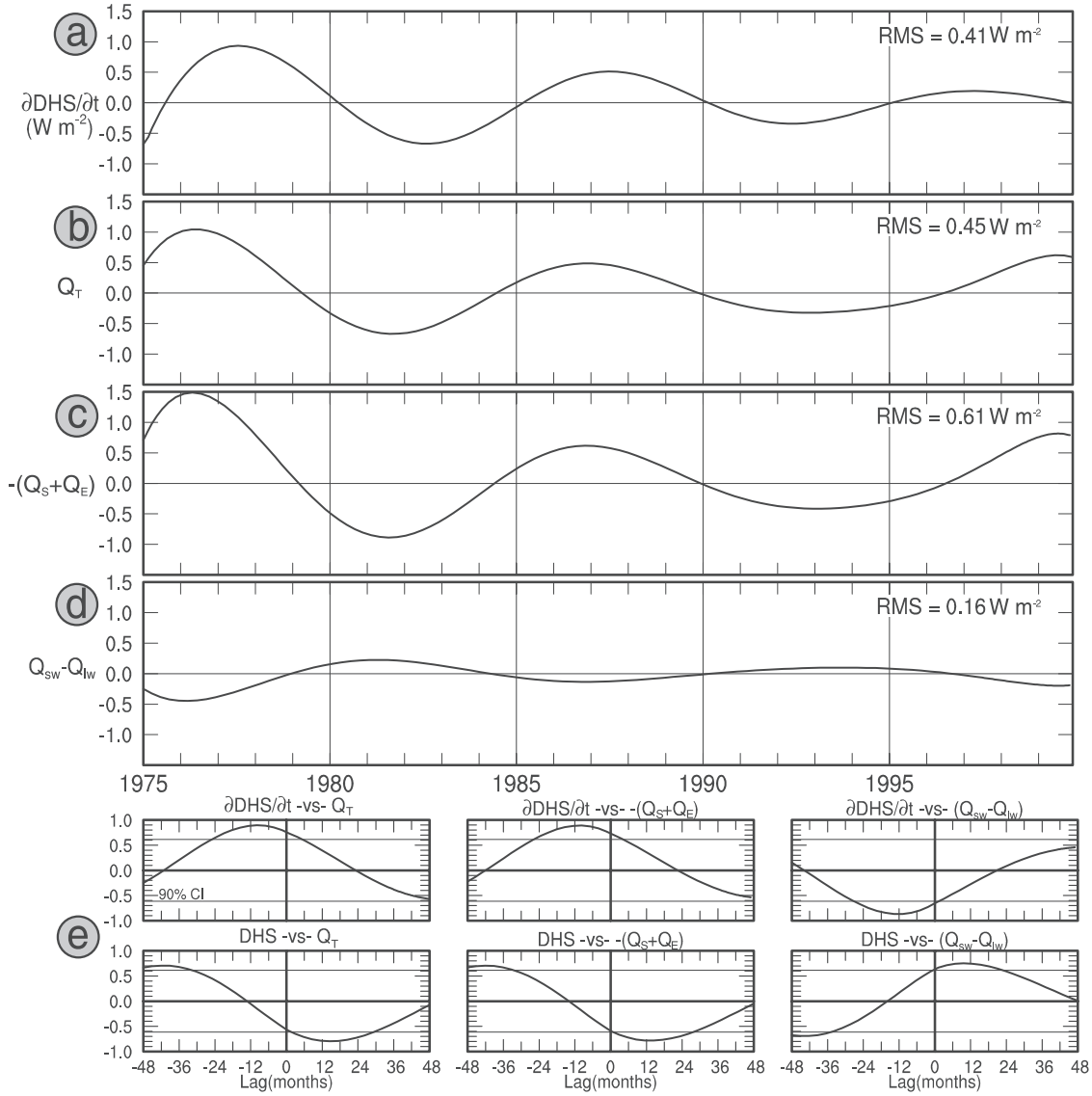

Figure 5. Time sequences of global tropical quasi-decadal anomalies of (a) ∂DHS/∂t, (b) total air-sea heat flux (Q_T), (c) sensible-plus-latent heat flux into the ocean [$-(Q_S + Q_E)$], and (d) net shortwave-minus-longwave heat flux ($Q_{SW} - Q_{LW}$) over the 25-year record. (f) Temporal lag cross correlations between both DHS and ∂DHS/∂T anomalies and Q_T, $-(Q_S + Q_E)$, and ($Q_{SW} - Q_{LW}$) anomalies, with $\sim$6 effective degrees of freedom assigned to the 90% confidence level of 0.6 [*Snedecor and Cochran*, 1980].

This is represented with the following linearized DHS budget equation;

$$\partial\left[\int\int(\mathrm{DHS}'\mathrm{dxdy})\right]/\partial t = -\,\mathrm{K}\int\int(\mathrm{DHS}')\mathrm{dxdy} + \int\int(\mathrm{Q_T}')\mathrm{dxdy} - \int\int(\overline{\mathrm{V}}_\mathrm{Y}\partial\mathrm{DHS}'/\partial_\mathrm{y} + \mathrm{V_Y}'\partial\overline{\mathrm{DHS}}/\partial\mathrm{y})\mathrm{dxdy} \quad (1)$$

where the prime designates anomalies and the overbar represents the mean. In equation (1), the double integral represents the area average over the tropical global ocean from 30°S to 30°N; DHS′ represents the diabatic heat storage anomaly; K^{-1} represents the *e*-folding dissipation timescale; Q_T' represents the total air-sea heat flux anomaly; and $\overline{V}_Y$ (V_Y') represents the mean (anomalous) meridional velocity component in the upper ocean. The mean meridional velocity component is composed of geostrophic-plus-Ekman components in the upper layer. The anomalous meridional velocity component relies only on the Ekman component, computed from the anomalous wind stress anomalies (see below). The anomalous geostrophic component remains unmeasured, but is assumed to be negligible in the upper layer, as determined in a realistic ocean general circulation model (OGCM) simulation of the anomalous DHS budget on interannual period scales [*White et al.*, 2001].

8.1. Global Tropical Total Air-Sea Heat Flux Anomaly

[21] We plot the time sequence of the anomalous DHS tendency on the left-hand side of equation (1) (Figure 5a) together with the total air-sea heat flux anomaly on the right-hand side (Figure 5b). We find these two variables

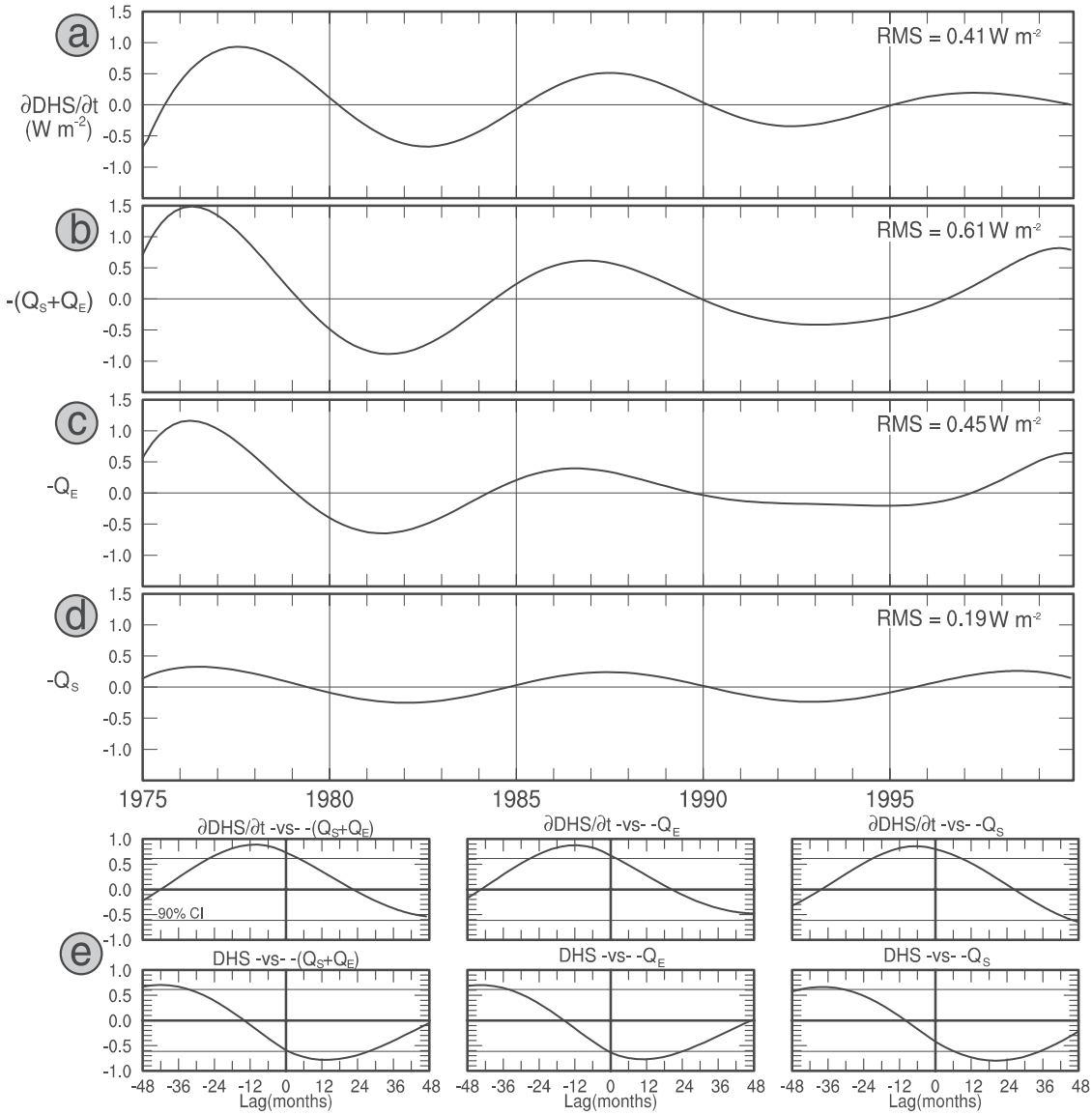

Figure 6. Time sequences of global tropical quasi-decadal anomalies of (a) ∂DHS/∂t, (b) latent-plus-sensible heat flux into the ocean [$-(Q_S + Q_E)$], (c) latent heat flux component into the ocean ($-Q_E$), and (d) sensible heat flux component into the ocean ($-Q_S$), over the 25-year record. (f) Temporal lag cross correlations between both DHS and ∂DHS/∂T anomalies and $-(Q_S + Q_E)$, $-Q_E$, and $-Q_S$ anomalies, with ~6 effective degrees of freedom assigned to the 90% confidence level of 0.6 [*Snedecor and Cochran*, 1980].

positively correlated at 0.90 over the 25-year record, the latter leading the former by 6 to 12 months (Figure 5e). We also find the dissipation of the DHS anomaly on the right-hand side of equation (1) positively correlated with the net total air-sea heat flux anomaly on the right-hand side at 0.80, the latter lagging the former by 12–18 months (Figure 5e). Thus the total air-sea heat flux anomaly drives the anomalous DHS tendency prior and during the onset of tropical warming, while acting as a source of dissipation during and following tropical warming, heating the overlying atmosphere. This situation differs from that observed on interannual period scales [*White et al.*, 2001] where the total air-sea heat flux anomaly did little to drive the anomalous DHS tendency during the onset of tropical warming, relegated instead to heating the overlying atmosphere.

[22] Here, the anomalous DHS tendency on the left-hand side of equation (1) can be seen ranging over ±0.9 W m^{-2} with an RMS variability of 0.41 W m^{-2}, while the total air-sea heat flux anomaly on the right-hand side ranges over ±1.0 W m^{-2} with an RMS variability of 0.45 W m^{-2}. These estimates of the RMS variability are not significantly different from one another. The separation of the total air-sea heat flux anomaly into its turbulent and radiative air-sea heat flux components [that is, $-\int\int(Q_S' + Q_E')dxdy$ and $\int\int(Q_{SW}' - Q_{LW}')dxdy$, respectively] finds them ranging over ±1.5 W m^{-2} and ±0.5 W m^{-2}, respectively (Figures 5c and 5d). Temporal lag cross correlations (Figure 5e) find the turbulent air-sea heat flux anomalies positively correlated with the total air-sea heat flux anomalies, while the radiative air-sea heat flux anomalies are negatively correlated, both

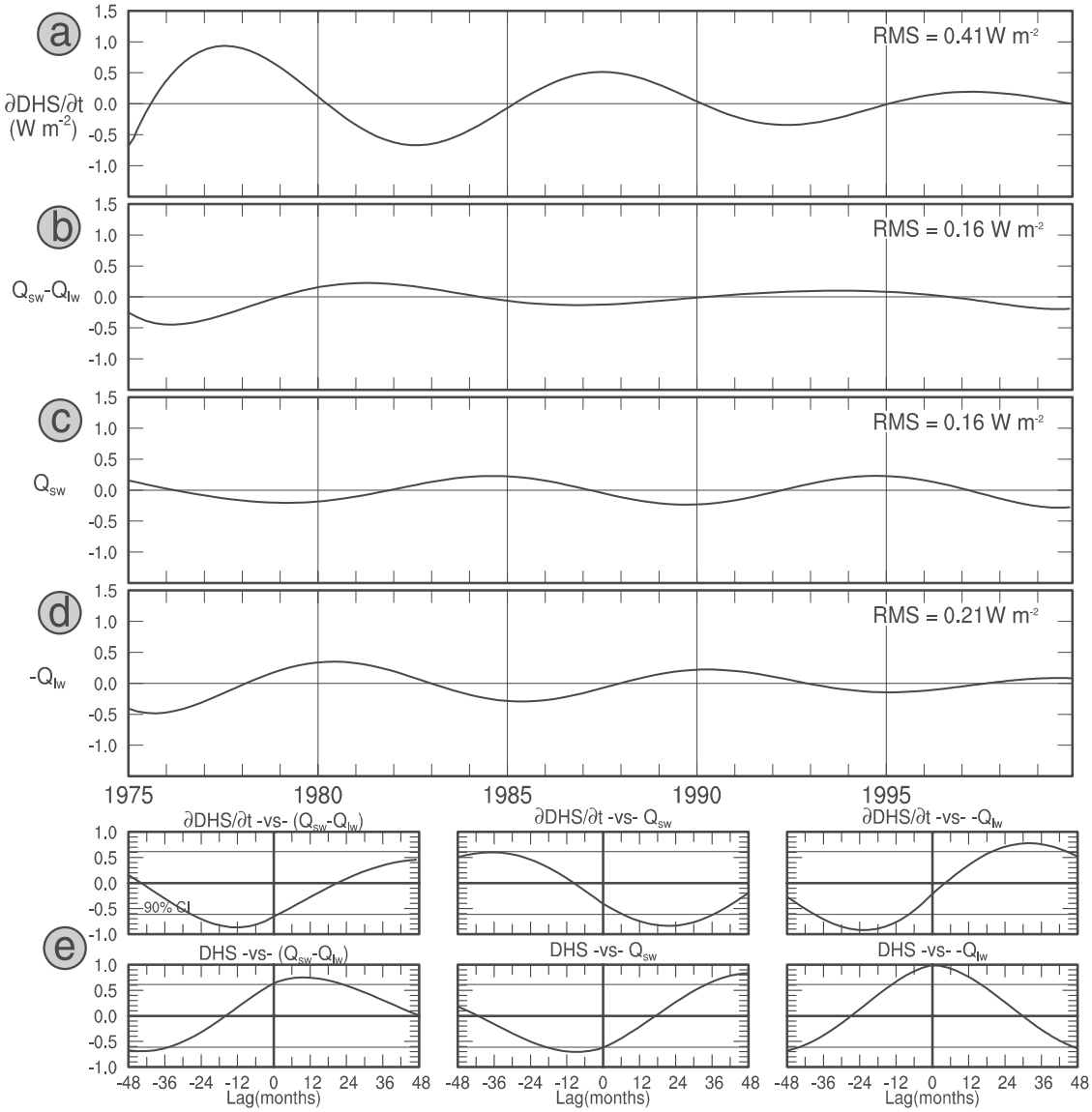

Figure 7. Time sequences of global tropical quasi-decadal anomalies of (a) ∂DHS/∂t, (b) net radiative heat flux ($Q_{SW} - Q_{LW}$), (c) the shortwave heat flux (Q_{SW}), and (d) the longwave heat flux ($-Q_{LW}$) over the 25-year record. (f) Temporal lag cross correlations between both DHS and ∂DHS/∂T anomalies and ($Q_{SW} - Q_{LW}$), Q_{SW}, and $-Q_{LW}$ anomalies, with ~6 effective degrees of freedom assigned to the 90% confidence level of 0.6 [*Snedecor and Cochran*, 1980].

directly out of phase with one another. Thus the total air-sea heat flux anomaly is dominated by its latent-plus-sensible heat flux component, which is directly out of phase with the weaker shortwave-minus-longwave heat flux component.

[23] Since the turbulent air-sea heat flux anomalies in Figure 5 are composed of latent-plus-sensible heat flux components, we separate the influence of the two components (Figure 6). The latent heat flux anomalies range over ±1.5 W m^{-2} (Figure 6c) with an RMS variability of 0.45 W m^{-2}, while the sensible heat flux anomalies range over ±0.3 W m^{-2} (Figure 6d) with an RMS variability of 0.19 W m^{-2}, about half as large. Thus the anomalous turbulent heat flux (Figure 6b) is dominated by the latent heat flux component (Figure 6c), both of which correlate positively with the anomalous DHS tendency at 0.90, the former leading the latter by 6 to 12 months (Figure 6e).

[24] Since net radiative air-sea heat flux anomalies in Figure 5 are composed of shortwave-minus-longwave heat flux components, we separate their respective influences (Figure 7). The shortwave and longwave radiative heat flux components can be seen fluctuating nearly out of phase with one another (Figures 7c and 7d), with the longwave heat flux component only slightly larger than the shortwave heat flux component, with RMS variability of 0.21 and 0.16 W m^{-2}, respectively. Thus the anomalous net radiative air-sea heat flux (Figure 7b) nearly resembles the longwave heat flux component (Figure 7d), but is displaced by a positive lead of 1–3 years stemming from the shortwave heat flux component (Figure 7c). This is confirmed by temporal lag

cross correlations between the anomalous DHS tendency and the anomalous net radiative air-sea heat flux and its two components (Figure 7e).

[25] Thus the increase in global tropical cloud cover during tropical warming (Figures 3 and 4) decreased the global tropical shortwave heat flux anomaly into the ocean (Figure 7a), accompanied by an even larger decrease in global tropical longwave heat flux anomaly out of the ocean (Figure 7d). As such, the net effect of this increase in cloud cover on the net radiative air-sea heat flux anomaly does not lend itself to simplistic statements; for example, reducing the net radiative heat flux into the ocean. Whereas the cloud cover is anomalously high prior to and during tropical warming in DHS anomaly (Figure 4), the net radiative heat flux into the ocean is anomalous high (Figure 7e).

[26] Moreover, the increase in global tropical trade wind intensity during the onset of tropical warming (Figures 3 and 4) can now be seen to be associated with an increase in sensible-plus-latent heat flux into the global tropical ocean (Figure 6e), heating the upper ocean. This indicates that the latter was influenced little by the increase in anomalous wind speed in the bulk formula of the sensible-plus-latent heat flux anomalies [*Cayan*, 1992]. Rather, the latter was driven primarily by the warm surface air temperature and moist specific humidity anomalies. Since the global tropical ZSW anomaly goes to zero during tropical warming (Figure 4f), the upward sensible-plus-latent heat flux derives from the warmer SST and more moist surface saturated specific humidity. Thus, on decadal period scales the anomalous sensible-plus-latent heat flux depends more on the anomalous air-sea temperature and specific humidity differences, and less on the anomalous wind speed.

8.2. Global Tropical Meridional Heat Advection Anomaly

[27] Now we estimate the mean net meridional advection of the anomalous DHS into and out of the global tropical ocean across 30°S to 30°N due to the mean geostrophic-plus-Ekman flow in the upper layer. The mean geostrophic flow was computed from the global distribution of the mean dynamic height (0/2000 m) based upon an analysis of all the available vertical density profiles collected over the global ocean by the National Oceanographic Data Center (NODC) during the 25-year record [*Levitus and Boyer*, 1994; *Levitus et al.*, 1994]. The mean Ekman flow was computed from the mean surface wind stress field over the global ocean [*Lagerloef et al.*, 1999] from the NCEP reanalysis conducted over the same period [*Kalnay et al.*, 1996]. This allows us to compute the $-\int\int(\overline{V}_Y\partial DHS'/\partial y)dxdy$ term on the right-hand side of equation (1). However, the magnitude of this term was so small (i.e.,< 0.1 W m^{-2}) that we do not display it. This indicates that the net mean meridional advection of DHS anomalies into and out of the global tropical ocean contributed negligibly to the anomalous integrated DHS budget therein.

[28] Next, we estimate the anomalous net meridional advection of the mean DHS into and out of the global tropical ocean from 30°S to 30°N due to the anomalous meridional Ekman transport in the upper layer (Figure 8b). We compute the meridional Ekman flow from anomalous zonal and meridional surface wind stress components (τ^X and τ^Y respectively) from the NCEP reanalysis [*Kalnay et al.*, 1996], with $V_Y' = (-f\tau^X + A\tau^Y)/(H(f^2 + A^2))$. In this latter equation, H represents the depth of the Ekman layer; *f* represents the Coriolis parameter; and A represents the Rayleigh friction coefficient in the oceanic momentum balance. The Rayleigh friction yields downwind flow near the equator as the Coriolis parameter goes to zero. We take H = 60 m and A = 2.2×10^{-5} s^{-1}, the latter estimated by linear regression analysis with near-surface drifter measurements [*Lagerloef et al.*, 1999]. This allows us to compute the $-\int\int(V_Y'\partial\overline{DHS}/\partial y)dxdy$ term on the right-hand side of equation (1).

[29] We plot the anomalous net meridional heat advection anomaly (Figure 8b) together with the anomalous DHS tendency (Figure 8a), the former ranging over ±0.7 W m^{-2} with an RMS variability of 0.42 W m^{-2} and the latter ranging over ±0.9 W m^{-2} with an RMS variability of 0.41. The temporal lag cross correlation has the net meridional heat advection anomaly positively correlated with the anomalous DHS tendency at 0.90 at a lag of ~3 years (Figure 8f). This indicates that the net meridional heat advection anomaly has only a weak influence on the anomalous DHS tendency. Rather, its principal role is to offset the dissipation of the anomalous DHS (Figure 8c) during tropical warming.

8.3. Net Global Tropical Heat Flux Anomaly

[30] Now we are in position to compute the net global tropical heat flux anomaly on the right-hand side of equation (1) (Figure 8e) by summing the net meridional heat advection anomaly (Figure 8b), the net heat dissipation anomaly (Figure 8c), and the net air-sea heat flux anomaly (Figure 8d). We compute the dissipation constant K in equation (1) by least squares estimation, i.e., minimizing the mean square of the differences between the right-hand and left-hand sides of equation (1). This yields a dissipation timescale $K^{-1} = 1.8$ years and allows the anomalous heat dissipation to range over ±0.5 W m^{-2} with an RMS variability of 0.22 W m^{-2}. This estimated dissipation of the anomalous DHS is expected to arise from the cross isopycnal mixing at the depth of the 22°C isotherm depth in the upper portion of the main pycnocline [*White et al.*, 2001]. The magnitude of the heat dissipation anomaly is ~1/2 that of the net meridional heat advection anomaly and the net air-sea heat flux anomaly on the right-hand side of equation (1), the latter two terms yielding RMS variability of 0.42 and 0.45 W m^{-2}, respectively.

[31] Summing the anomalous global tropical heat fluxes on the right-hand side of equation (1) produces the net global tropical heat flux anomaly over the 25-year record, ranging over ±1.0 W m^{-2} with an RMS variability of 0.39 W m^{-2} (Figure 8e). This is similar to the anomalous DHS tendency on the left-hand side of equation (1), which ranges over ±0.9 W m^{-2} with an RMS variability of 0.41 W m^{-2}. Moreover, the temporal lag cross correlations finds the anomalous DHS tendency on the left-hand side of equation (1) positively correlated with the net heat flux anomaly on the right-hand side of equation (1) at 0.6 at a 6 month lead. Within this anomalous DHS balance, the total air-sea heat flux anomaly (with an RMS variability of 0.45 W m^{-2}) (Figure 8d) acts principally to drive the anomalous DHS warming tendency over the global tropical ocean (Figure 8a). Within the total air-sea heat flux anomaly, the downward sensible-plus-latent heat flux anomaly

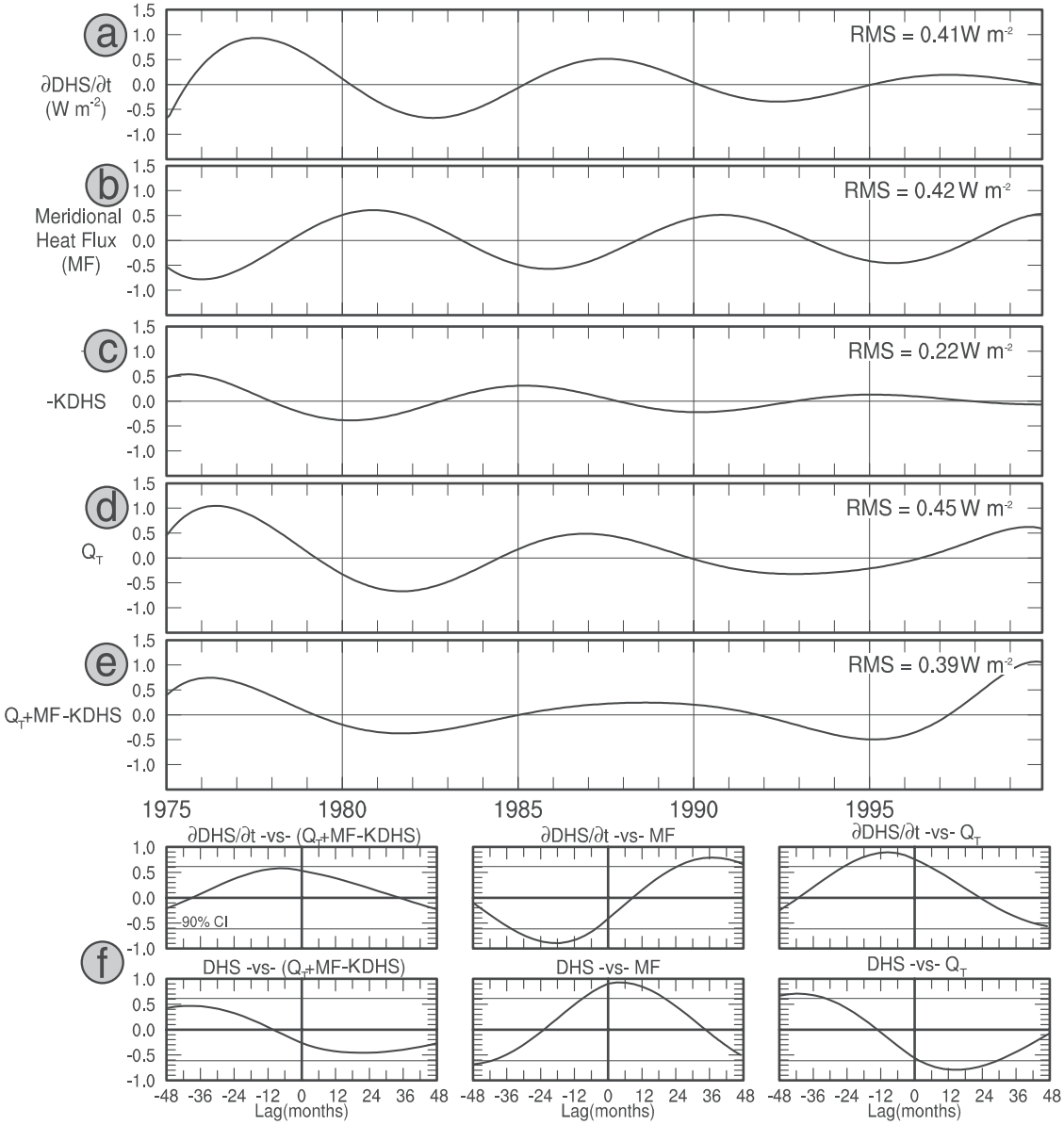

Figure 8. Time sequences of global tropical quasi-decadal anomalies of (a) ∂DHS/∂t on the left-hand side of equation (1) and (b) the net meridional heat advection into the tropical ocean across 30°S and 30°N (MF), (c) the net dissipation of DHS anomaly (−KDHS), and (d) the net total air-sea heat flux (Q_T) on the right-hand side of equation (1) over the 25-year record. Also displayed is (e) the net global tropical heat flux anomaly from all sources (i.e., Q_T + MF − KDHS) on the right-hand side of equation (1) over the 25-year record. (f) Temporal lag cross correlations are computed between both DHS and ∂DHS/∂T anomalies and MF, Q_T, and (Q_T + MF − KDHS) anomalies, with ∼6 effective degrees of freedom assigned to the 90% confidence level of 0.6 [*Snedecor and Cochran*, 1980].

(Figure 5c) overwhelms the tendency by a weaker upward shortwave-minus-longwave heat flux anomaly to drive a DHS cooling tendency (Figure 5d). The net meridional heat advection anomaly with an RMS variability of 0.42 W m^{-2} (Figure 8b) acts principally to balance the loss of DHS anomaly during tropical warming, including that estimated to mix into the deep ocean via cross-isopycnal mixing (with an RMS variability of 0.22 W m^{-2}) and the smaller portion lost to the atmosphere through upward total air-sea heat flux anomaly (Figures 8c and 8d). The net meridional heat advection anomaly also yields a weak anomalous DHS cooling tendency during the onset of tropical warming, which like the upward shortwave-minus-longwave heat flux anomaly, reduces the anomalous DHS warming tendency by the downward sensible-plus-latent heat flux anomaly.

9. Discussion and Conclusions

[32] We find the quasi-decadal signal in the global tropical NCEP SST anomaly larger than the global tropical SIO SST anomaly by a factor of ∼1.5 over the 25-year record. When we correct for this underestimation in the quasi-decadal DHS and DAT anomalies, we find the global tropical quasi-decadal SIO DAT anomalies ranging over

±0.10°C, the same as for global tropical quasi-decadal SIO SST anomalies. This finding is consistent with the hypothesis that the anomalous heating of the upper ocean on decadal period scales extends throughout the upper layer of the ocean to the depth of the 22°C isotherm [*White et al.*, 1997], the latter outcropping near 30° latitude. This definition of DHS and DAT anomalies (i.e., extending from the sea surface to the depth of the 22°C isotherm in the upper portion of the main pycnocline) yields an anomalous global tropical DHS tendency ranging over ±0.9 W m^{-2}. This is nearly an order of magnitude larger than the surface radiative forcing of ±0.1 W m^{-2} associated with the ~11-year signal in the Sun's surface radiative forcing. However, it is within 10% of the sum of the anomalous net heat flux on the right-hand side of equation (1) contributing to the anomalous DHS tendency on the left-hand side.

[33] Diagnosing the global tropical DHS budget associated with the global quasi-decadal signal of *Allan* [2000] and *Tourre et al.* [2001], we find the anomalous DHS warming tendency with an RMS variability of 0.41 W m^{-2} driven principally by the downward sensible-plus-latent heat flux anomaly into the global tropical ocean with an RMS variability of 0.61 W m^{-2}. This warming by the atmosphere overwhelms the tendency by weaker upward shortwave-minus-longwave heat flux anomaly to drive an anomalous DHS cooling tendency with an RMS variability of 0.16 W m^{-2}. The total air-sea heat flux anomaly that drives the anomalous DHS warming tendency has an RMS variability of 0.45 W m^{-2}, both variables larger near the beginning of the record and weaker toward the end of the record for reasons unknown. During tropical warming, the estimated dissipation of DHS anomaly with an RMS variability of 0.22 W m^{-2} into the deep ocean and a similar loss of DHS anomaly to the overlying atmosphere through upward total air-sea heat flux is balanced by a decrease in the net poleward Ekman heat advection out of the tropics, with an RMS variability of 0.42 W m^{-2}.

[34] So, even though the anomalous global-averaged DAT and DHS tendencies of ±0.10°C and ±0.9 W m^{-2}, respectively, are phase-locked to changes in the Sun's irradiance [*White et al.*, 1998], they appear to occur as a consequence of internal mechanisms within the quasi-decadal signal in the Earth's ocean-atmosphere-land system. We arrive at this conclusion on the heels of work by *White et al.* [2001], who found anomalous global tropical DAT and DHS tendencies of ±0.15°C and ±1.6 W m^{-2}, respectively, occurring on interannual period scales (i.e., encompassing the global signals associated with ENSO) in the absence of interannual signals in the Sun's surface radiative forcing. Moreover, here we find the intensity of the ~11-year signal in the Sun's surface radiative forcing of ~0.1 W m^{-2} to be half an order of magnitude smaller than the corresponding anomalous DHS tendency in the global tropical ocean.

[35] Initially, we expected the global interannual and quasi-decadal signals to produce global tropical DAT and DHS tendencies for the same reasons. However, we found the global tropical warming/cooling in both signals occurring for very different reasons. On interannual period scales, the reduction in global tropical trade winds occurs during the onset of tropical warming (i.e., during the onset of El Niño), driving the anomalous DHS warming tendency by reducing the net meridional Ekman heat advection out of the tropics. On decadal period scales, tropical warming occurs ~2 years before the tropical warm phase, with an increase in global tropical trade winds occuring during the onset of tropical warming. Instead, the anomalous DHS warming tendency arises from the downward sensible-plus-latent heat flux anomaly, wherein air temperature (specific humidity) anomalies are warmer (more moist) than the sea surface temperature (saturated specific humidity) anomalies. However, during both interannual and quasi-decadal tropical warming, the anomalous total air-sea heat flux is upward, with the global tropical ocean heating the overlying atmosphere, and both experiencing a dissipation of warm DHS anomalies into the deep ocean via cross-isopycnal warming.

[36] Thus, on interannual period scales the global tropical upper ocean warms and then heats the overlying atmosphere, while on decadal period scales the global tropical atmosphere warms and then heats the underlying ocean. The question is whether the difference in the way the interannual and quasi-decadal global signals generates global warming/cooling arises simply from differences in period scale, or whether it arises from the fact that the quasi-decadal signal is phase locked to the ~11-year signal in the Sun's irradiance. It may be the latter, when we come to realize that the ~0.1% change in the Sun's total irradiance on decadal period scales is associated with a ~4% change in the Sun's ultraviolet (UV) portion of the total irradiance [*Lean et al.*, 1995b]. The latter has been shown by *Haigh* [1994, 1999] to be absorbed by stratospheric ozone in an atmospheric general circulation model, producing a 0.5°C warming of the air temperature in the lower stratosphere during peak solar irradiance, as observed by *Labitzke and van Loon* [1997]. This response is also accompanied by significant changes in both stratospheric and tropospheric winds. The question is whether the warmer air temperatures and higher specific humidities in the lower troposphere during the onset of quasi-decadal tropical warming, which appear to drive the downward sensible-plus-latent heat flux anomaly into the upper ocean, can be traced to the warming of the lower stratosphere by the UV portion of the Sun's total irradiance signal.

Appendix A: Diabatic Heat Storage Anomaly on Decadal Period Scales

[37] *White et al.* [1998] computed the anomalous diabatic heat storage ($T'\overline{H}$) in the upper layer of the ocean above the top of the main pycnocline. Therein, T' is the depth-averaged temperature (DAT) anomaly extending from the surface to some isotherm in the main pycnocline and $\overline{H}$ is the mean depth of that isotherm, different at each grid point. In the preset study we compute the anomalous DHS down to the depth of the 22°C isotherm. This choice of isotherm arises from consideration of the depth to which the quasi-decadal heating signal penetrates into the global ocean through subduction from isopycnals outcroping into the near surface mixed layer near 30°N in winter. *Kleeman et al.* [1999] has shown in the Pacific Ocean that the mean geostrophic flow can advect upper ocean temperature anomalies from the subtropics into the tropics along isopycnal surfaces. We conducted an experiment with the SIO upper ocean temperature reanalysis data set, computing the anomalous global tropical DHS tendency with respect to the top of the main pycnocline and with respect to the 26°C,

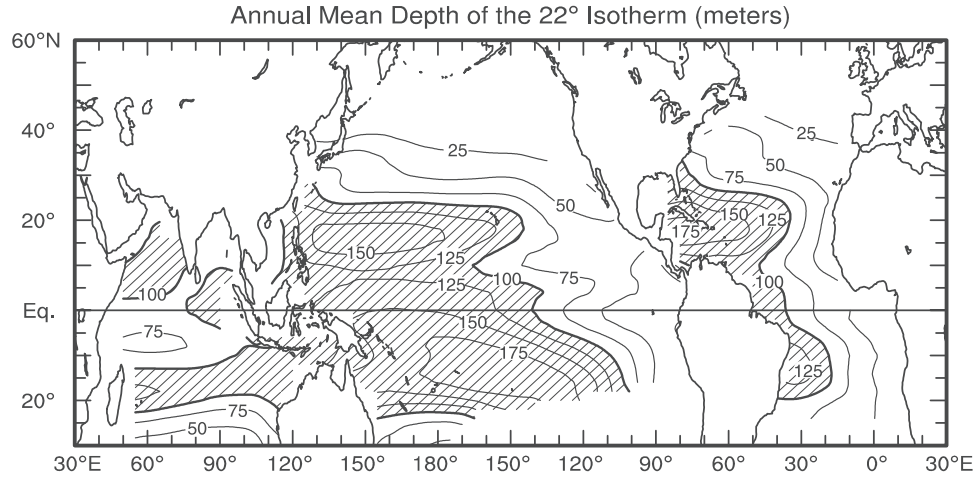

Figure A1. Global distribution of the mean depth of the 22°C isotherm, taken from the SIO upper ocean temperature reanalysis [*White et al.* [2001]. The contour interval is 25 m, and depths greater than 100 m are hatched.

22°C, and 18°C isotherms, all of which outcrop into the winter near-surface mixed layer between 20° and 40° latitude. Plotting the magnitude of these quantities versus the isotherm to which each is computed yields RMS estimates of 0.16, 0.29, 0.41, and 0.46 W m^{-2}, respectively. So, the magnitude of this quantity tends to asymptote near 22°C. Even larger estimates of anomalous global tropical DHS tendencies, associated with even deeper isotherms, were found unable to correlate with global tropical total air-sea heat flux anomaly from 30°S to 30°N. This is because these isotherms outcrop poleward of the tropical and subtropical domain from 30°S to 30°N in winter.

[38] The geographical distribution of the mean depth ($\overline{H}$) of the 22°C isotherm at each grid point (Figure A1) finds it

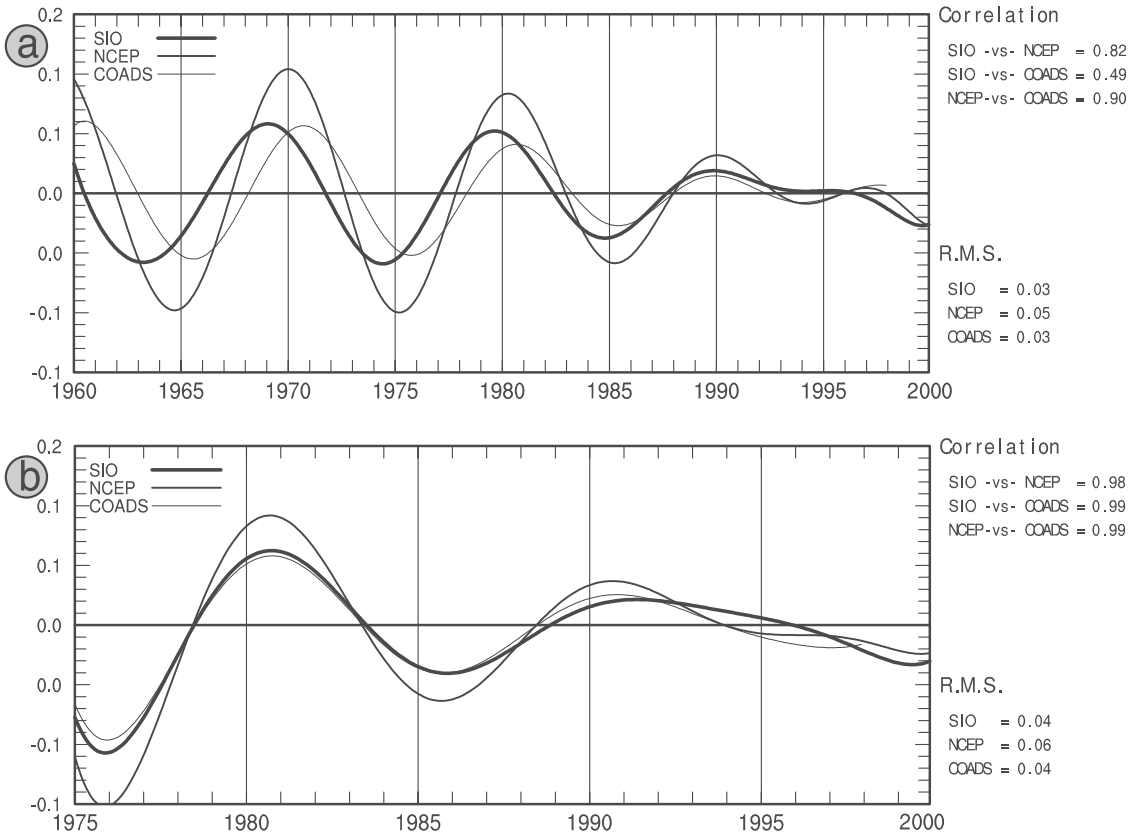

Figure B1. (a) Time sequences of global tropical quasi-decadal SST anomalies over the epoch from 1960 to 2000, computed from the NCEP, COADS, and SIO reanalysis data sets. (b) Same as in Figure B1a but for the epoch 1975–2000. Cross correlations among the three time sequences in each panel are given to the right, together with the RMS of the global tropical SST anomalies.

outcropping into the near-surface mixed layer of ~50 m depth in winter near 30° latitude in both hemispheres. This makes it useful for capturing the anomalous heat in the layer above it over this latitude domain. Its deepest penetration (100 to 175 m) occurs near the middle of the shallow anticyclonic gyres between 10° and 20° latitude in the three ocean basins in both hemispheres.

Appendix B: Comparison of SIO, NCEP, and COADS Global-Averaged SST Anomalies

[39] We plot the global tropical quasi-decadal SST anomalies (Figure B1) from the SIO reanalysis [*White et al.*, 2001], from the NCEP reanalysis [*Kalnay et al.*, 1996], and from the COADS reanalysis [*Slutz et al.*, 1985; *Woodruff et al.*, 1993]. This is conducted over two epochs, from 1960 to 2000 (Figure B1a) and from 1975 to 2000 (Figure B1b), with anomalies in each epoch computed from means in each.

[40] For the epoch from 1960 to 2000, the RMS of the global tropical NCEP SST anomalies of 0.05°C was larger than those of the global tropical COADS and SIO SST anomalies of 0.03°C by a factor of ~1.7 (Figure B1a). Inspection of these time sequences indicate that most of this difference occurred before 1985, corresponding to the onset of routine expendable bathythermograph (XBT) sampling over the global ocean during the TOGA/WOCE program [*White*, 1995]. This underestimation of the global tropical SIO SST anomalies prior to 1985 was due to relatively poor sampling of temperature profiles over the tropical global ocean [*White*, 1995] compared with the relatively dense sampling of surface marine weather observations [*Kalnay et al.*, 1996]. Moreover, prior to 1985, the alignment of the three estimates of global tropical quasi-decadal SST anomalies can be seen to have been poor (Figure B1a).

[41] For the epoch from 1975 to 2000, the RMS of global tropical NCEP SST anomalies of 0.06°C remains larger than those of global tropical COADS and SIO SST anomalies of 0.04°C by a factor of ~1.5 (Figure B1b). However, inspection of these time sequences finds the three estimates of global tropical SST anomalies to be much better aligned than over the longer epoch (Figure B1a), with cross correlations among the three estimates > 0.98. Even so, underestimation of the global tropical SIO SST anomalies by a factor of 1.5 occurs throughout most of this period.

[42] **Acknowledgments.** This research was supported by the National Aeronautics and Space Administration (NASA) under contracts NAG5-7096 in support of the World Ocean Circulation Experiment (WOCE) program and NAG5-12465 in support of the Living With a Star (LWS) program. Dan Cayan and Mike Dettinger are supported by the U.S. Geological Survey's Global Change Hydrology Program. Warren White and Dan Cayan are supported by the Scripps Institution of Oceanography. Our thanks extend to Ted Walker who provided the computational and visualization support and to Andrea Fincham who prepared the final figures. Our thanks extend to Jeffrey Park who made important contributions to the discussion on the statistical significance of these results.

References

Allan, R. J., ENSO and climatic variability in the last 150 years, in *El Niño and the Southern Oscillation: Multiscale Variability, Global and Regional Impacts*, edited by H. F. Diaz and V. Markgraf, pp. 3–55, Cambridge Univ. Press, New York, 2000.

Andersen, N., On the calculation of filter coefficients for maximum entropy spectral analysis, *Geophysics*, *39*, 69–72, 1974.

Cayan, D., Variability of latent and sensible heat fluxes estimated using bulk formulae, *Atmos. Oceans*, *30*, 1–62, 1992.

Haigh, J. D., The role of stratospheric ozone in modulating the solar radiative forcing of climate, *Nature*, *370*, 544–546, 1994.

Haigh, J. D., A GCM study of climate change in response to the 11-year solar cycle, *Q.J.R. Meteorol. Soc.*, *125*, 871–892, 1999.

Kalnay, E., et al., NCEP/NCAR 40-year reanalysis project, *Bull. Am. Meteorol. Soc.*, *77*, 437–471, 1996.

Kaylor, R. E., Filtering and decimation of digital time series, *Tech. Rep. Note BN 850*, Pys., Sci., and Tech., Univ. of Md., College Park, 1977.

Kleeman, R., J. P. McCreary, and B. A. Klinger, A mechanism for generating ENSO decadal variability, *Geophys. Res. Lett.*, *26*, 1743–1746, 1999.

Labitzke, K., and H. van Loon, The signal of the 11-year sunspot cycle in the upper troposphere-lower stratosphere, *Space Sci. Rev.*, *80*, 393–410, 1997.

Lagerloef, G. S. E., G. Mitchum, R. Lukas, and P. Niiler, Tropical Pacific near-surface currents estimated from altimeter, wind and drifter data, *J. Geophys. Res.*, *104*, 23,313–23,326, 1999.

Lau, K.-M., and H. Weng, Climate signal detection using wavelet transform: How to make a time series sing, *Bull. Am. Meteorol. Soc.*, *76*, 2391–2402, 1995.

Lean, J. L., J. Beer, and R. Bradely, Reconstruction of solar irradiance since 1610: Implications for climate change, *Geophys. Res. Lett.*, *22*, 3195–3198, 1995a.

Lean, J. L., O. R. White, and A. Skumanich, On the solar ultraviolet irradiance during the Maunder Minimum, *Global Biogeochem. Cycles*, *9*, 171–182, 1995b.

Levitus, S., and T. Boyer, *World Ocean Atlas 1994*, vol. 4, *Temperature, NOAA Atlas NESDIS*, vol. 3, 129 pp., Natl. Oceanic and Atmos. Admin., Silver Spring, Md., 1994.

Levitus, S., R. Burgett, and T. Boyer, *World Ocean Atlas 1994*, vol. 3, *Salinity, NOAA Atlas NESDIS*, vol. 3, 111 pp., Natl. Oceanic and Atmos. Admin., Silver Spring, Md., 1994.

Mann, M. E., and J. Park, Joint spatio-temporal modes of surface temperature and sea level pressure variability in the Northern Hemisphere during the last century, *J. Clim.*, *9*, 2137–2162, 1996.

Reid, G. C., Solar total irradiance variations and the global sea surface temperature record, *J. Geophys. Res.*, *96*, 2835–2844, 1991.

Slutz, R. J., S. J. Lubker, J. D. Hiscox, S. D. Woodruff, R. L. Jenne, D. H. Joseph, P. M. Steurer, and J. D. Elms, *Comprehensive Ocean-Atmosphere Data Set; Release 1*, 268 pp., Environ. Res. Lab., Natl. Oceanic and Atmos. Admin., Boulder, Colo., 1985.

Snedecor, G. W., and W. G. Cochran, *Statistical Methods*, 507 pp., Iowa State Univ. Press, Ames, 1980.

Tourre, Y. M., B. Rajagopalan, Y. Kushnir, M. Barlow, and W.B. White, Patterns of coherent decadal and interdecadal climate signals in the Pacific Basin during the 20th century, *Geophys. Res. Lett.*, *28*, 2069–2072, 2001.

Weare, B., and J. Nasstrom, Examples of extended empirical orthogonal function analysis, *Mon. Weather Rev.*, *110*, 481–485, 1982.

White, W. B., Design of a global observing system for basin-scale upper ocean temperature changes, *Prog. Oceanogr.*, *36*, 169–217, 1995.

White, W. B., Tropical coupled Rossby waves in the Pacific ocean-atmosphere system, *J. Phys. Oceanogr.*, *30*, 1245–1264, 2000.

White, W. B., and D. R. Cayan, A global ENSO wave in surface temperature and pressure and its inter-decadal modulation from 1900 to 1997, *Geophys. Res.*, *105*, 11,223–11,242, 2000.

White, W. B., J. Lean, D. R. Cayan, and M. Dettinger, A response of global upper ocean temperature to changing solar irradiance, *J. Geophys. Res.*, *102*, 3255–3266, 1997.

White, W. B., D. R. Cayan, and J. Lean, Global upper ocean heat storage response to radiative forcing from changing solar irradiance and increasing greenhouse gas/aerosol concentrations, *J. Geophys. Res.*, *103*, 21,355–21,366, 1998.

White, W. B., D. R. Cayan, M. Dettinger, and G. Auad, Sources of global warming in upper ocean temperature during El Niño, *J. Geophys. Res.*, *106*, 4349–4367, 2001.

White, W. B., Y. M. Tourre, M. Barlow, and M. Dettinger, A delayed action oscillator shared by biennial, interannual, and decadal signals In the Pacific basin, *J. Geophys. Res.*, *108*(C3), 3070, doi:10.1029/2002JC001490, 2003.

Woodruff, S. D., S. J. Lubker, K. Wolter, S. J. Worley, and J. D. Elms, Comprehensive Ocean-Atmosphere Data Set Release 1a; 1980–92, *Earth Syst. Monit.*, *4*, 1–8, 1993.

Young, H. D., *Statistical Treatment of Experimental Data*, 172 pp., McGraw-Hill, New York, 1962.

Zebiak, S. E., and M. A. Cane, A model El Niño–Southern Oscillation, *Mon. Weather Rev.*, *115*, 2262–2278, 1987.

W. B. White, Scripps Institution of Oceanography, University of California at San Diego, La Jolla, CA 92093-0230, USA. (wbwhite@ucsd.edu)

M. D. Dettinger and D. R. Cayan, United States Geological Survey, San Diego, CA 92123, USA.